Photocatalytic CO_2 Reduction to Methanol Integrated with the Oxidative Coupling of Thiols to S-X (X=S, C) bond formation over $Fe_3O_4/BiVO_4$ Composite

Nitish Saini[a,b], Sandhya Saini[a,b], Santanu Majumder,[c]*Kyra Sedransk Campbell,[d] Suman L Jain[a]*

[a]*Chemical & Material Sciences Division, CSIR-Indian Institute of Petroleum, Haridwar Road, Mohkampur, Dehradun-248005, India*
[b]*Academy of Scientific and Innovative Research, Ghaziabad- 201002, India*
[c]*Faculty of Science and Technology, Bournemouth University, Talbot Campus, Fern Barrow, Poole, BH12 5BB, UK*
[d]Department of Chemical and Biological Engineering, University of Sheffield, Sheffield, S1 3JD, UK
**Email: suman@iip.res.in; smajumder@bournemouth.ac.uk*

Abstract

A dual functional approach for CO_2 reduction coupled with oxidative organic synthesis in a single reaction system is a promising way to get CO_2 reduction products with the co-production of high-value chemicals using light energy under mild conditions. Herein, we report an integrated approach in which CO_2 acts as an oxidant that affords the oxidative homocoupling of thiols to disulfides and cross-coupling with organohalides to thioethers along with the simultaneous production of methanol over a heterostructured composite of iron (III) oxide and bismuth vanadate ($Fe_3O_4/BiVO_4$) under visible light irradiation. The developed protocol provides an economical and fascinating organic synthesis combined with methanol production by simultaneously utilising photo-excited electrons and holes more efficiently in a single reaction system. Hence, the present study opens up new opportunities for solar fuel generation from CO_2 integrated with the synthesis of value-added fine chemicals.

Keywords: Photocatalysis, CO_2 reduction, thiol, methanol, coupling reaction

Introduction

Development of new approaches to valorise carbon dioxide (CO_2) for the production of fuels and chemicals are capturing significant attention from government, industry, and the research community.[1,2] Among the known CO_2 mitigation strategies, catalytic reduction of CO_2 into fuel and chemicals including both conversion into gaseous products (for example, CO, CH_4, and C_2H_4) and liquid products (for example, HCOOH, CH_3OH, and C_2H_5OH) has gained significant interest in recent years.[3-8] A common drawback of these conversions is the required coupling of CO_2 reduction with the oxidation of water to establish a carbon neutral cycle and to convert solar energy to chemical energy.[9] Photocatalytic materials used for this process include semiconductors (for example, metal oxides, mixed metal oxides, heterojunctions and organic semiconductors); molecular complexes of transition metals (such as Ru, Ir, Re, Ni, Fe) have been reported to drive multi-electron CO_2 reduction *via* H_2O as the proton and electron donor.[10-12] However the kinetically sluggish oxidation half-reaction ($2H_2O/4e^- + 4H^+ + O_2$) in most of the known systems resulted to the low activity and poor durability. To achieve the efficient CO_2 reduction in these systems, sacrificial electron donors (*e.g.* ascorbic acid, triethanolamine (TEOA), triethylamine) are required to serve as hole scavengers; this approach limits the overall economic viability.[13] Other challenges are also often cited: inefficient use of the oxidizing power of photogenerated holes[14]; additional cost of the sacrificial reagents; unwanted oxidation products limit the practical applicability of CO_2 reduction process.[15] Hence, there is a scope to develop a solar-light-driven integrated system for CO_2 photoreduction combined with the oxidation of an organic substrate.

Here we report an efficient CO_2 photoreduction integrated with oxidation of thiols under visible light, enabling the efficient utilization of the excited electrons and holes to simultaneously produce methanol and disulfides in a single reaction system. The oxidation of

thiols to produce disulfides is an important transformation as these compounds find wide applications in the chemical industry, pharmaceutical and biological domains mainly as structural motifs in various bioactive compounds as well as in drug delivery systems (Figure 1).[16-18]

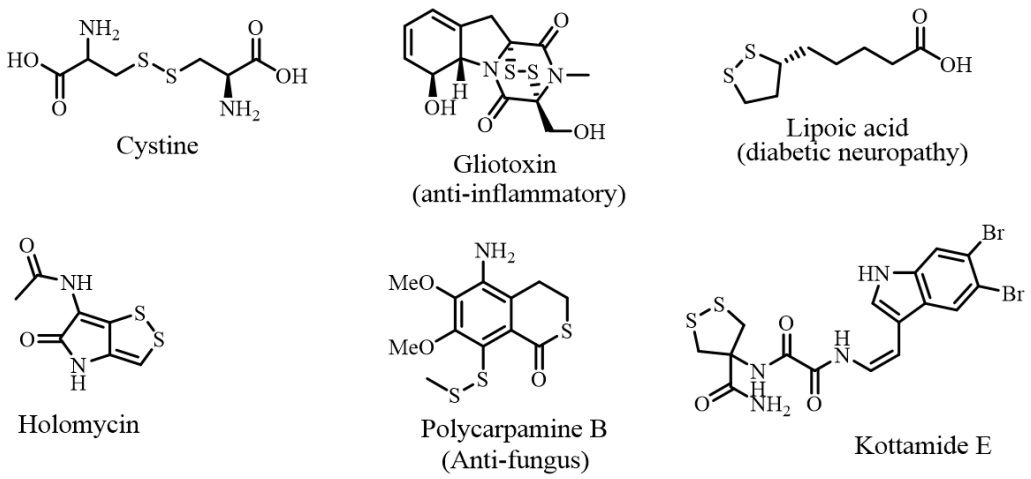

Figure 1. Sulfur compounds of biological importance

Apart from the conventional stoichiometric oxidants which produce copious amounts of undesirable metallic wastes, a number of catalytic methods using molecular oxygen as oxidant (*e.g.*, O_2) have been reported in the presence of base.[19] Most of the known methods are associated with the drawbacks of using expensive catalytic systems, higher reaction temperature, and over oxidation. Recently photocatalytic route has been presented as a sustainable approach for the selective conversion of thiols to high-value disulfides; the advantages over the above mentioned traditional thermal catalytic approaches include mild reaction condition requirements and the use of solar energy. A few catalysts such as $Mn(CO)_5Br$,[20] $Cu_2(OH)PO_4$[21] and metal-free Eosin Y[22] have been demonstrated with O_2 as oxidant for this transformation. A further extension of this concept has included Ni(II)/CdSe QDs mediated photoredox dehydrogenation of thiols to disulfides coupled with the hydrogen production.[23] The cross-coupling of thiols with organohalides to produce corresponding thioethers has also been demonstrated.[24, 25] The reported methods suffer from the drawbacks

of using expensive noble metals and homogeneous catalysis. By contrast, the photocatalytic synthesis of these compounds using transition metal complexes, *e.g.*, $Ru(bpy)_3Cl_26H_2O$,[26] [fac-$Ir(ppy)_3$],[27] have only recently been reported. However, to the best of our knowledge, a photoredox system that effectively integrates CO_2 reduction with the oxidation of thiols to produce disuldifes and thioethers has never been demonstrated.

Here, we firstly report a heterostructured $Fe_3O_4/BiVO_4$ composite photocatalyzed CO_2 reduction to methanol integrated with the oxidative coupling of thiols to produce S-X (X=S, C)-coupled products under visible light irradiation at atmospheric pressure and ambient temperature (Scheme 1).

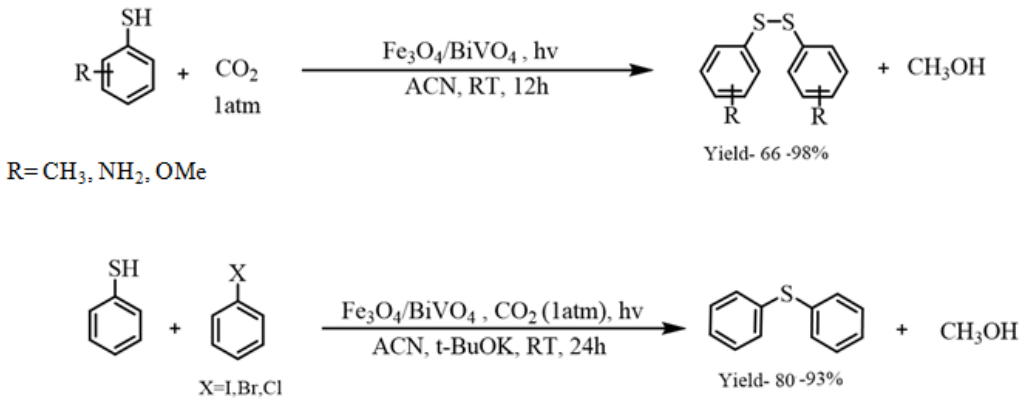

Scheme 1: Light assisted oxidative coupling of thiols to S-X bond formation (X=S, C)

Experimental section

All the chemicals used for the synthesis of Fe_3O_4, $BiVO_4$ and $Fe_3O_4/BiVO_4$ composites were readily available and used as received. The individual components Fe_3O_4 and $BiVO_4$ were prepared by following the reported literature procedures.[28, 29]

Synthesis of the heterostructured $Fe_3O_4/BiVO_4$ composites

In a typical synthesis, a mixture of $Bi(NO_3)_3.5H_2O$ (4.84 gm) and NH_4VO_3 (1.17 gm) in 20 mL water (H_2O) was stirred for 24 h and then the resulting solution was sonicated for 1h for

the uniformity of the solution. In the subsequent step, 600 mg (0.6 gm) of $Fe(NO_3)_3$. $9H_2O$ was added to the above solution and the resulting solution was stirred for 24 h. The obtained yellow precipitates were collected *via* filtration and washed thoroughly with water, ethanol and finally dried at 60 ^oC under vacuum overnight. The obtained yellow solid was then calcined in muffle furnace at 300 ^oC for 4h and the resulting final material was named as FBV-2 photocatalyst. For the comparison, other composites i.e., FBV-1 and FBV-3 were synthesized by varying the amount of $Fe(NO_3)_3.9H_2O$ as 500 mg (0.5 gm) and 700 mg (0.7 gm) respectively.

Photocatalytic oxidative coupling of thiols to S-X (X=S, C) bond formation

In a typical experiment, thiophenol (1mmol) and acetonitrile (5 ml) were taken in a 50 ml vessel and the mixture was evacuated and purged with N_2 for several times to remove any dissolved O_2. Subsequently, the photocatalyst FBV-2 (20 mg) was added, and the resulting mixture was purged with CO_2 for 30 min and equipped with a CO_2-filled balloon. The reaction vessel was tightly closed and irradiated for 12 h by 20W white LED light (λ> 415 nm, Model No- HP-FL-20W-F-Hope LED optoelectric Co., Ltd). After reaction, the photocatalyst was recovered by filtration and the filtrate was analyzed by GC-FID and GC-MS to determine the conversion and the selectivity of the products. For the cross coupling reaction of thiophenol with iodobenzene equimolar amount of base KO^tBu was used under otherwise identical conditions for 24 h of reaction time. The CO_2 photoreduction product methanol was quantified by GC-FID (Perkin-Elmer, stibwaxCP Sil 24CB LOW BLEED/MS 30 mm, flow rate of 0.5 mL min^{-1}, injector temperature 330 °C and FID detector temperature 350 °C). However, the selectivity and identity of the coupling products was confirmed by GC-MS analysis (*See Supporting Information*).

Characterization techniques

The stretching and bending vibrations in all samples were measured by Fourier transform infrared spectroscopy (FT-IR) on a Perkin-Elmer spectrum RX-1 IR spectrophotometer with a potassium bromide window at room temperature in the range of 4000-400 cm^{-1}. Raman spectra were measured by using a HORIBA Scientific instrument equipped with OLYMPUS confocal microscope. A He/Ne power source laser with a wavelength of 633 nm was used for excitation and 2 mW laser power was used to record the spectra. X-ray diffraction (XRD) patterns were acquired on a Bruker D8 Advance diffractometer at 40 kV, 40 mA, and Cu Kα radiation (λ = 0.15418nm) to ascertain the crystallinity of the materials with a scan rate of 0.02 °/s, the analysis covered the scan range of 2θ = 2º to 80º. The morphological features were probed using a field emission scanning electron microscope (FESEM) (JEOL JSM7610F) fitted with an EDS (Oxford Instruments). By mounting the ethanol dispersed sample on a Lacey carbon-coated Cu grid, a JEM 2100 (JEOL, Japan) microscope was used to conduct high-resolution transmission electron microscopy (HR-TEM). The absorption spectra of the samples were determined by UV-VIS spectroscopy using $BaSO_4$ as a reference on a Perkin Elmer Lambda 750 UV-VIS-NIR spectrophotometer with a 10-mm quartz cell. X-ray photoelectron spectroscopic (XPS) analysis was done on the KRATOS AXIS 165 and Mg Kα irradiation, to investigate the oxidation state and binding energy of the elements in the synthesized photocatalysts. The N_2 adsorption-desorption isotherms were carried out on Micromeritics ASAP 2020 Surface Area & Porosity Analyzer. The BET specific surface areas were determined from the adsorption data in the relative pressure (P/P_o) range of -0.1 to 1.1.

Results & discussion

Synthesis and characterization of the photocatalysts

The individual components Fe_3O_4, $BiVO_4$ and their heterostructured composites were synthesized as given in the experimental section. The prepared materials were characterized by various analytical techniques. Figure 2A display the FTIR spectra of the magnetite Fe_3O_4, $BiVO_4$, FBV-1, FBV-2 and FBV-3. In all case a broad band at 3430 cm^{-1} is attributed to the water molecules adsorbed on the surface of the materials. In $BiVO_4$, the band at 683 cm^{-1} is attributed to the Bi-O vibration and the bands in the region of 925 cm^{-1} to 758 cm^{-1} are assigned to V-O bending and stretching vibrations, respectively.[30] In bare Fe_2O_3 two intense peaks represented by yellow region at around 500 cm^{-1} are attributed to the Fe-O bond stretching vibration mode in the crystalline lattice.[31] The bands at 1643 cm^{-1} and 3436 cm^{-1} are related to the hydroxyl groups due to OH-bending and stretching vibrations respectively.[32] In the prepared composites FBV-1, FBV-2 and FBV-3, the appearance of new bands in the region of 1530 cm^{-1} to 1235 cm^{-1} along with the observance of Fe-O, Bi-O and V-O bands confirmed the interaction of both Fe_3O_4 and $BiVO_4$ in the synthesized Fe_3O_4/$BiVO_4$ composites (Figure 2A).

Further, the Raman spectra of the materials are shown in Figure 2B. In Fe_3O_4, the band at 301.66 cm^{-1} is attributed to T_{1g} mode.[33] In the hybrids (FBV-1, FBV-2, and FBV-3), an intense band at 823.33 cm^{-1} is assigned to the symmetric V-O stretching mode.[30] The band at 352.5 cm^{-1} is attributed to symmetric or anti-symmetric bending modes of vanadate anion (VO_4^{3-}) in Fe_3O_4/$BiVO_4$ composites.[34] The bands in the region 100-250 cm^{-1} are attributed to the Fe-O bending and stretching mode of vibrations. Hence, the presence of the V-O, VO_4^{3-}, and Fe-O modes further confirmed the successful formation of the Fe_3O_4/$BiVO_4$ composites.

The phase purity and crystallinity of the materials i.e., Fe_3O_4, FBV-1, FBV-2 and FBV-3 was probed by XRD as shown in Figure 2C. For Fe_3O_4 (brownish black colour), the diffraction

peaks are in good agreement with the standard JCPDS card No. 00-002-1035,[35] which is assigned to magnetite mineral having space group Fd-3m and cubic crystal structure with cell parameters a= 8.41 A°. In the prepared composites i.e. FBV-1, FBV-2, and FBV-3, the peaks at 2θ values and respective planes are in good agreement with $BiVO_4$ phase having tetragonal crystal system (JCPDS No. 00-014-0688).[36,37] The existence of Fe_3O_4 peaks in the hybrid composites confirmed the successful formation of the $Fe_3O_4/BiVO_4$ hybrids. Moreover, the concentration of the Fe in the hybrids did not affect the crystallinity of the material.

The SEM images of Fe_3O_4 nanoparticles (Figure 2Di-ii) reveal irregular crystalline forms and the agglomeration of many ultrafine particles because of their small size and magnetism, this is consistent with other literature observations.[38] The SEM images of FBV-2 (Figure 2D iii-iv), clearly shows crystalline microstructures of $BiVO_4$, which are sintered together with the spherical Fe_3O_4 nanoparticles.

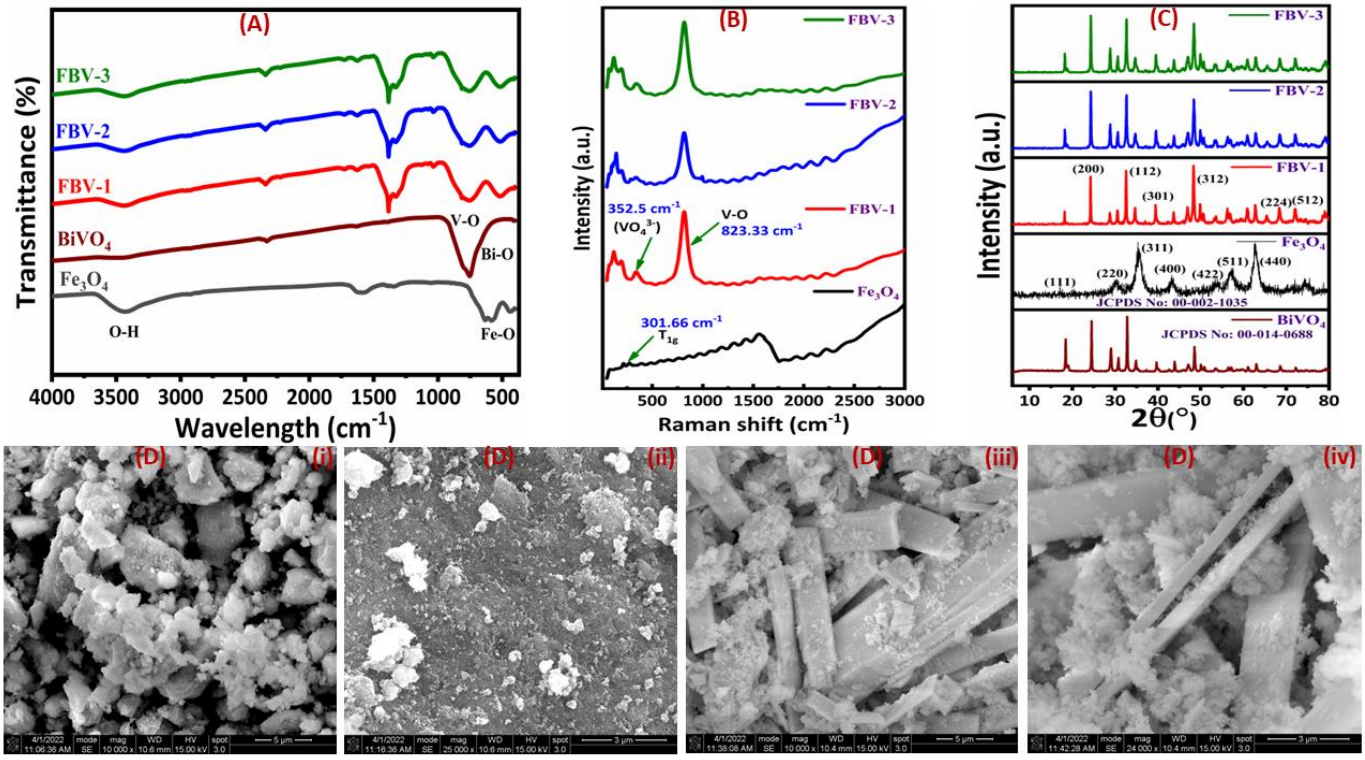

Figure 2: (A) FTIR; (B) Raman; (C) XRD; and (D) SEM images of Fe_3O_4 (i-ii), FBV-2 (iii-iv)

The topographical, morphological, and crystalline behaviour of the active photocatalyst FBV-2 was studied by high resolution transmission electron microscopy (HR-TEM) analysis. The TEM images of FBV-2 are shown in Figure 3 (a, b), which confirms that Fe_3O_4 is spherical in shape and connected to $BiVO_4$ crystals. The distance between the fringes d = 2.03 A^o is attributed to plane (400) with respect to Fe_3O_4 and d = 3.37 A^o, 2.35 A^o is assigned to crystal planes (200), (301) of $BiVO_4$ at 10 nm scale. The SAED pattern (Figure 3c) suggests the polycrystalline nature of the heterostructured composite FBV-2 having crystal planes (111), (200), (301), (400), (512), and (440) corresponding to the d values 4.06 A^o, 3.37 A^o, 2.35 A^o, 2.03A^o, 1.28 A^o, and 1.14 A^o, respectively. The planes (111), (400), and (440) are related to Fe_3O_4 and the plane (200), (301), and (512) are related to $BiVO_4$, respectively.[39] The presence of all the desired elements i.e., Fe, Bi, V, and O is confirmed by EDX analysis (Figure 3d). Moreover, elemental mapping confirmed the homogeneous distribution of all the constituents in the FBV-2 composite as shown in Figure 4.

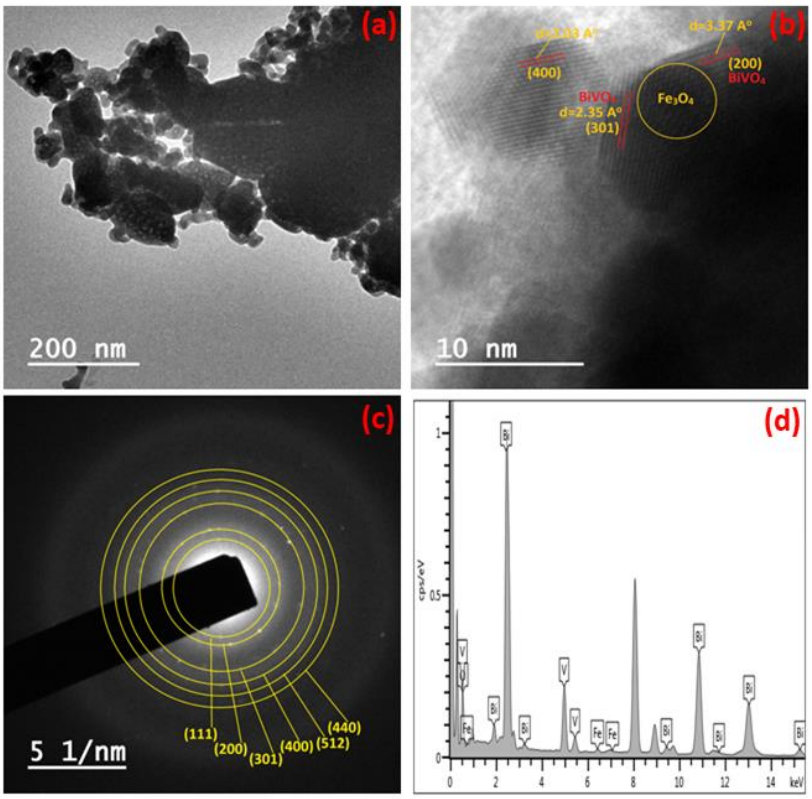

Figure 3: a,b) HR-TEM images; c) SAED pattern and d) EDX of the photocatalyst FBV-2

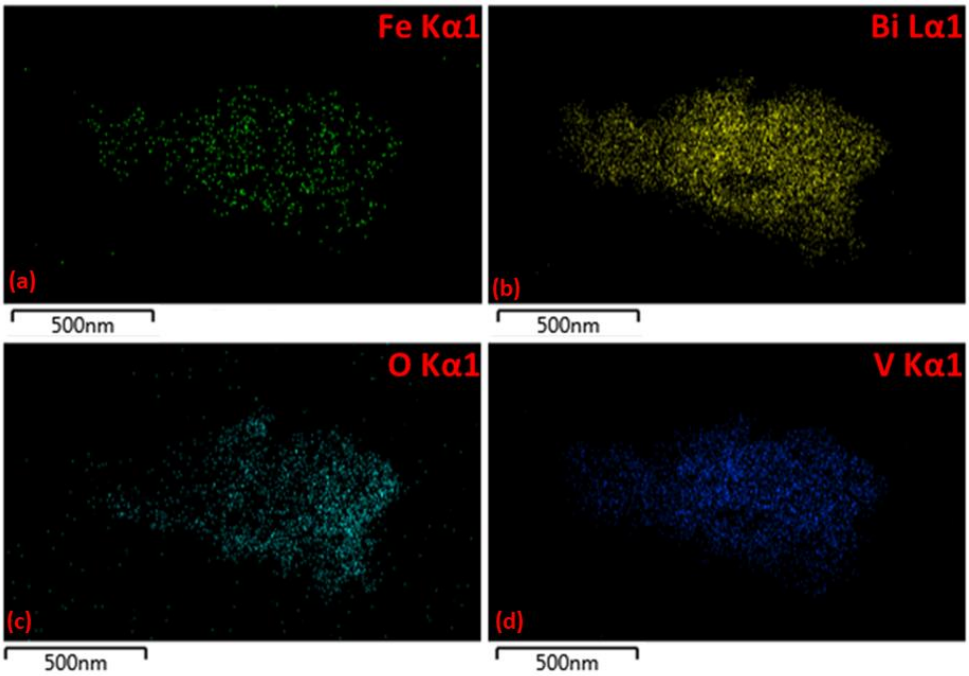

Figure 4: Elemental mapping of the synthesised photocatalyst FBV-2

X-ray photoelectron spectroscopy (XPS) was used to measure the elemental composition of the surface, oxidation states and binding states of the elements in pristine Fe_3O_4 and active photocatalyst FBV-2. Figure 5a shows the XPS survey scan of FBV-2, confirming the existence of all the desired elements in the active photocatalyst. The Fe 2p XPS spectra (Figure 5b) deconvoluted into two peaks at 724.76 eV and 709.65 eV, corresponding to the Fe $2p_{1/2}$ and $Fe2p_{3/2}$ core levels, which confirms that Fe present in Fe^{2+} and Fe^{3+} oxidation states.[40] The Bi 4f spectra (Figure 5c) is deconvoluted into four peaks, in which two are related to Bi $4f_{5/2}$ core level at 163.90 eV and the other two are related to Bi $4f_{7/2}$ core level at 158. 60 eV, respectively.[41] For V 2p (Figure 5d), the XPS spectra is deconvoluted into two peaks having core levels V $2p_{1/2}$ and $V2p_{3/2}$ at 523. 70 eV and 516.22 eV; along with O1s, which is further deconvoluted into two peaks corresponding to the binding energies, 528.62 eV and 532.43 eV, confirming the formation of V-O bond.[42] O1s XPS spectra (Figure 5e) is deconvoluted into three peaks corresponding to the binding energies 531.63 eV (O-H), 529.53 eV (Fe-O), and 529.32 eV (V-O), respectively.[42]

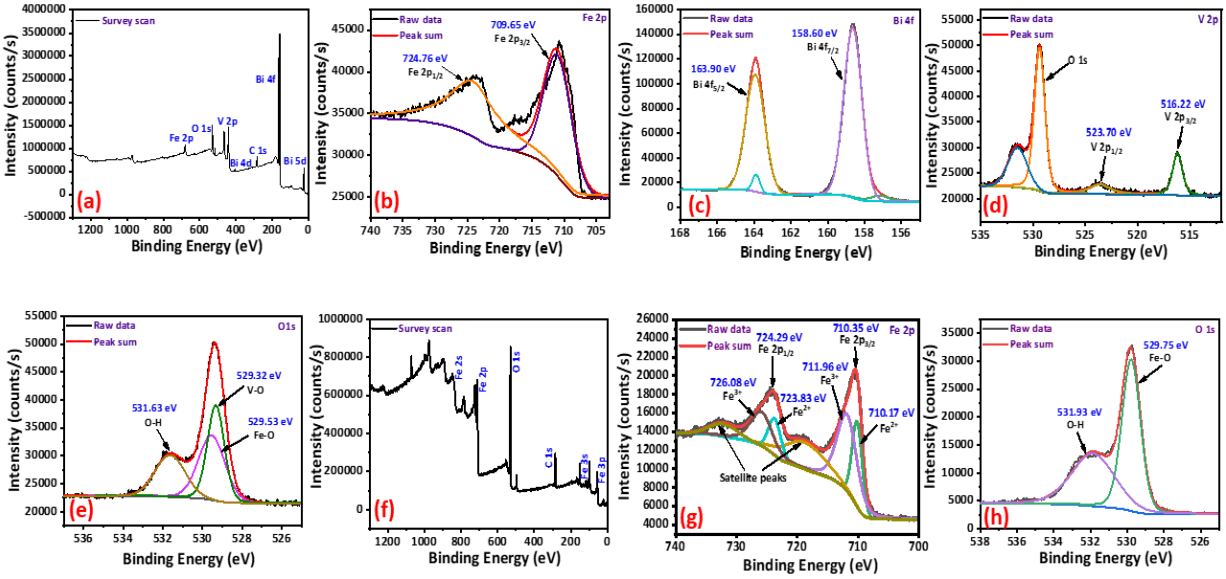

Figure 5: XPS spectra of FBV-2, a) survey scan, b) Fe 2p, c) Bi 4f, d) V 2p, and e) O 1s; XPS spectra of Fe_3O_4, f) survey scan, g) Fe 2p, and, h) O 1s of Fe_3O_4

For the comparison, the XPS spectrum of Fe_3O_4 is also shown in Figure 5(f, g, and h). The XPS survey scan confirms the presence of Fe and O elements in the Fe_3O_4 (Figure 5f). The Fe 2p XPS spectra (Figure 5g) is deconvoluted into six peaks, out of which three are attributed to Fe $2p_{1/2}$ at binding energy 724.29 eV and the remaining three are assigned to Fe $2p_{3/2}$ at 710.35 eV, confirming that Fe is present in (2+) and (3+) oxidation states, respectively.[43] The peaks at 732.50 eV and 718.74 eV are attributed to satellite peaks due to Fe $2p_{1/2}$ and Fe $2p_{3/2}$ core levels related to the spin-orbital interaction in bare Fe_3O_4. O1s XPS spectra (Figure 5h) is deconvoluted into two peaks at binding energy 531.93 eV (O-H) and 529.75 eV(Fe-O).[44, 45] In comparison to the pristine Fe_3O_4, the shifting of the respective peaks in FVB-2 indicate the interaction between both components in the FBV-2 composite.

The optical properties of the materials ($BiVO_4$, Fe_3O_4, FBV-1, FBV-2, and FBV-3) were determined by UV-Vis spectroscopy (Figure 6a). In $BiVO_4$, two broad peaks at 250-350 nm and 350-500 nm are assigned to the ligand to metal (L-M) charge transfer transitions.[30] Similarly, in Fe_3O_4 a broad absorbance in the region between 200 to 700 nm is ascribed to ligand to metal charge transition.[46] As anticipated, higher absorbance in the visible region is

observed in all the heterostructured composites (FBV-1, FBV-2, and FBV-3), indicating the synergistic effect of both the components on photocatalytic activity. Importantly, the intensity of the visible light absorption increases with the Fe content in the composites due to the charge transfer transitions. Moreover, the band gap values for BiVO4, Fe_3O_4, FBV-1, FBV-2, and FBV-3 photocatalysts as calculated by Tauc plot are 2.47 eV, 1.42 eV, 2.40 eV, 1.61eV, and 2.19 eV, respectively (Figure 6b). Among all the materials, FBV-2 exhibited lowest band gap that confirmed its higher photocatalytic efficiency.

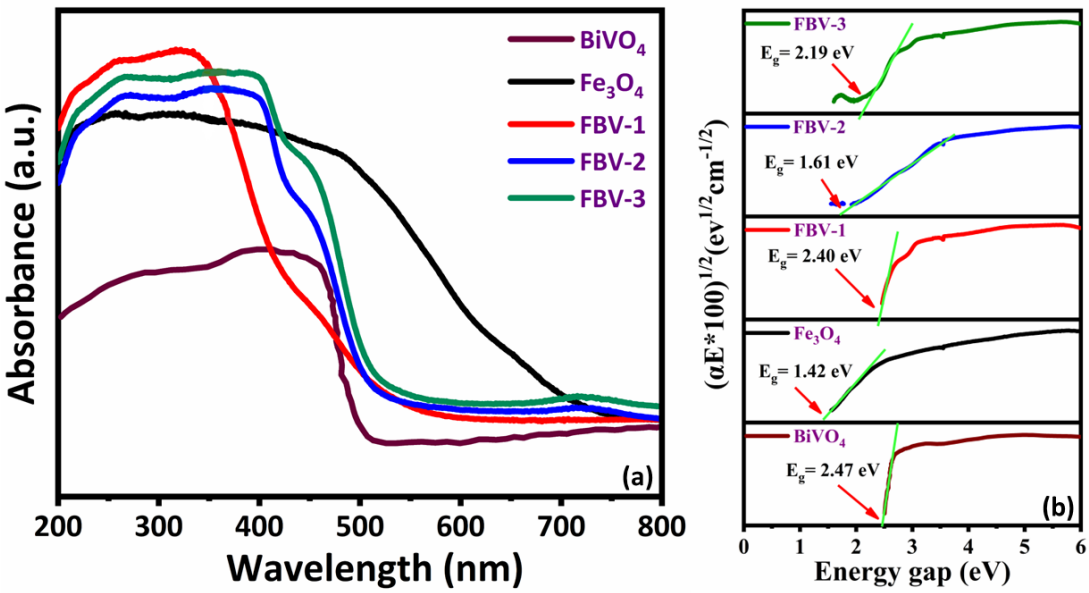

Figure 6: (a) UV-Vis; (b) Tauc plot of the $BiVO_4$, Fe_3O_4, FBV-1, FBV-2, and FBV-3

The Fe_3O_4 has a surface area S_{BET} = 22.30 m^2g^{-1} larger than the FBV compositions: FBV-2 (6.00 m^2g^{-1}) > FBV-3 (4.78 m^2g^{-1}) > FBV-1(3.56 m^2g^{-1}). The decrease in surface area could attribute to the increase in pore diameter in composites (FBV-1 (26.89 nm), FBV-2 (36.85 nm), FBV-3 (23.44 nm) as compared to bare Fe_3O_4 (11.93 nm).

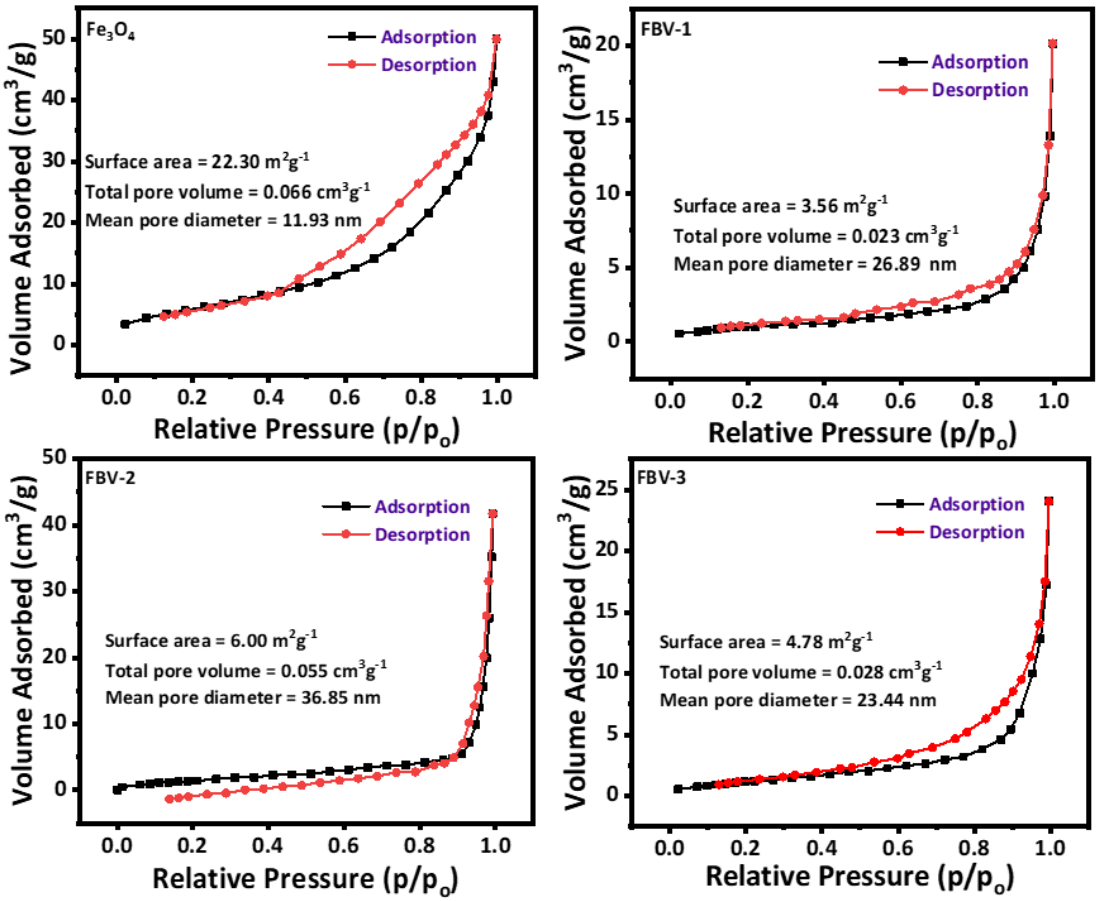

Figure 7: N_2 adsorption-desorption isotherm of the synthesised photocatalysts Fe_3O_4, FBV-1, FBV-2, and FBV-3

Photocatalytic reactions

The photocatalytic performance of synthesized materials, *i.e.*, Fe_2O_3 and FBV-1, FBV-2, FBV-3 composites, was initially tested for the oxidative coupling of thiophenol in acetonitrile solvent (a model substrate) using CO_2 (without added base) under visible-light irradiation for 12h. The individual components, Fe_3O_4 and $BiVO_4$, reached 28% and 42% yield, respectively, of the desired disulfide (Table 1, entry 1-2). The three composites all achieved higher yields, where FBV-2 reached 92% yield of diphenyl disulfide and 371µmol/g of methanol that is higher than that of FBV-1 (Table 1, entry $3^{i\text{-}iii}$). Further, the reduced photocatalytic efficiency on higher Fe loading in FBV-3 can be attributed to the reduced accessibility of the active sites to the substrate on the catalyst surface. The photocatalytic activity of Fe_3O_4@$BiVO_4$ (FBV) photocatalysts under visible-light illumination was higher than that of pure $BiVO_4$ owing to

the narrow band gap energy and delayed charge (electron-hole pair) recombination. Further, the incorporation of Fe_3O_4 reduces the band gap of FBV composites than the bare $BiVO_4$ that led to the higher visible light absorbance and enhanced photocatalytic efficiency. Moreover, Fe_3O_4 make the developed composite Fe_3O_4@$BiVO_4$ magnetic that facilitate the transfer and movement of the photogenerated electrons, resulting to higher separation efficiency of charge carriers. Further, to confirm that the synthesized FBV-2 was a composite, we performed a reaction using a physical mixture of 10% Fe_3O_4 with $BiVO_4$ under the optimized conditions (Table 1, entry 5). A significantly reduced disulfide yield (42%) %) in comparison to the FBV-2 (92%), confirming that the active photocatalyst FBV-2 was a composite. In the absence of light, there was no methanol formed, indicating that photogenerated electrons are required for the CO_2 photoreduction. However, a very poor yield of the disulfide was obtained in the absence of the light. Similarly, the reaction did not proceed in the absence of the photocatalyst. These results confirmed that the reaction is photocatalytic and both light and photocatalyst are required for this integrated synthesis. Alternative solvents for acetonitrile were considered, namely DMF and DMSO (both CO_2-philic solvents), but resulted in lower yields (Table 1, entry 6-7). The reaction did not proceed in non-polar solvents tested (benzene and carbon tetrachloride). The higher efficiency of the reaction in acetonitrile is likely due to (1) the higher solubility of CO_2 which can be achieved and (2) efficient photoreduction to methanol. In the absence of CO_2, under otherwise identical conditions, the yield of the corresponding disulfide reached 33%. There was no methanol detected in the absence of CO_2, confirming that photogenerated electrons are the key active species for the photoreduction of CO_2 to methanol in the developed photocatalytic system. Varying the mass of catalyst used, whilst keeping all others variables constant, resulted in a reduced yield (62%) of disulfide for a reduced catalyst loading (10 mg) and an increased yield (96%) for an increased catalyst loading (30 mg). A further increase to 40 mg of catalyst had an adverse effect on the yield;

one possible reason is the shielding effect of the photocatalyst that prevents the interaction of the CO_2 and thiol with the active sites. The optimized reaction conditions used were: 20 mg FBV-2 photocatalyst, acetonitrile, visible light and CO_2.

Table 1. Optimization of reaction conditions using thiophenol as a model substrate.[a]

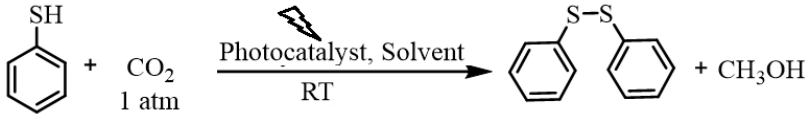

Entry	Catalyst	Solvent	Visible Light	Disulfide Yield(%)[b]
1	Fe_3O_4	ACN	yes	28
2	$BiVO_4$	ACN	yes	42
3[i]	FBV-1	ACN	yes	63
3[ii]	FBV-2	ACN	yes	92
3[iii]	FBV-3	ACN	yes	67
4	FBV-2	ACN	no	26
5	$^{10\%}Fe_3O_4/BiVO_4$	ACN	yes	42
6	FBV-2	DMF	yes	73
7	FBV-2	DMSO	yes	56
8[c]	FBV-2	ACN	yes	33

[a]**Reaction conditions:** thiophenol (1 mmol), photocatalyst (20 mg), solvent (5 ml), 20W LED light (λ = 415 nm), room temperature (26-28 ^{o}C) and 1 atm pressure, 12h [b]disulfide yield was determined by GC-MS, [c]without CO_2

After having the optimal experimental conditions, the reaction was generalized using various thiols and the results are summarized in Scheme 2.

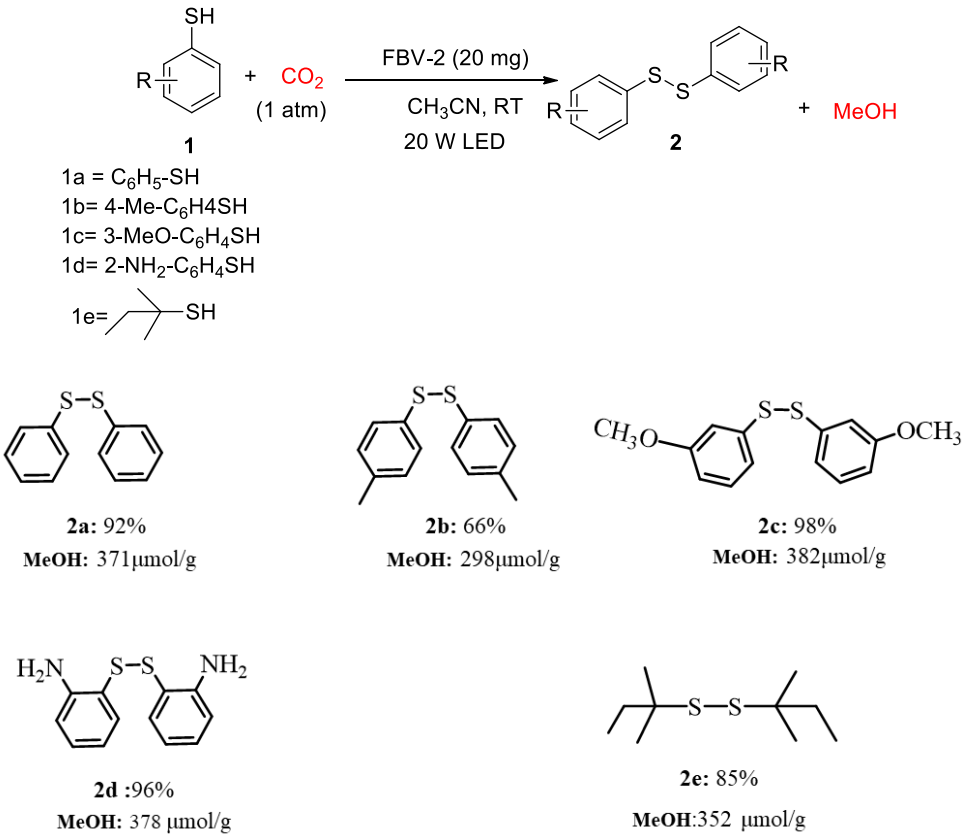

Scheme 2: FBV-2 catalyzed photoreduction of CO_2 integrated with oxidative coupling of thiols to disulfides

Under the developed protocol, all thiophenol derivatives with different substituents (-CH_3, CH_3O–, -NH_2,) **1b-1d** and aliphatic thiol **1e** converted smoothly and efficiently to the corresponding disulfides selectively without any by-product formation. Among the various substrates, excellent yield i.e., 98% was observed for 3-methoxy thiophenol along with the 382 µmol/g methanol being formed simultaneously from CO_2 reduction.

Further, the selected photocatalyst FBV-2 was tested for the cross coupling of thiophenol with iodobenzene in the presence of KO^{t}Bu as base under otherwise identical conditions. After the 24h of irradiation diphenyl sulphide was obtained selectively in 89% yield along with the CO_2 photoreduction product methanol (296 µmol/g) as confirmed by GC-MS and GC-FID, respectively.

The use of alternate bases, like K_2CO_3, TEA and DBU in place of KO^{t}Bu remained ineffective for the present reaction. The poor solubility of K_2CO_3 in acetonitrile and steric hindrance of TEA and DBU might be the reason of their ineffectiveness. Therefore, we have chosen KO^{t}Bu for further study. In the absence of base, the cross coupling reaction did not occur, instead we obtained corresponding disulfide from homo coupling thiophenol along with the unreacted iodobenzene.

The reaction was generalized with respect to altering the aromatic and aliphatic halides (Table 2). All the substrates successfully formed diphenyl sulphide in yields >80%. Among all the aryl halides, iodobenzene due to lower bond dissociation energy of C-I bond, has a higher product yield than bromo & chlorobenzene. Substituted iodobenzene, with an electron withdrawing group (-NO_2), resulted in a yield of 93% with the simultaneous production of methanol in 312 μmol/g (Table 2, entry 4). Heterocyclic and alkyl halo derivatives have also been utilized; their yields were generally inferior to the other candidate halides but still remained >80%.

Table 2. FBV-2 catalyzed cross coupling of thiols with organohalides using CO_2[a]

S. No	**Thiol**	**halide**	**Product**	**Yield (%)[b]**	**CH_3OH (μmol/g)[c]**
1	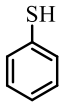	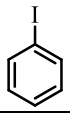	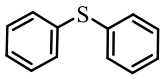	89	296
2	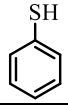		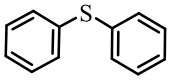	87	285
3	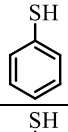		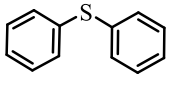	84	271
4	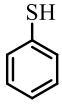	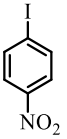	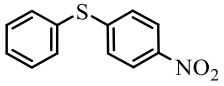	93	312
5	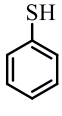	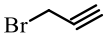	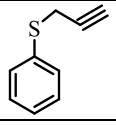	92	304

6	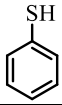		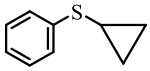	82	261
7	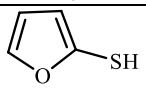	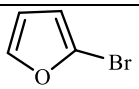	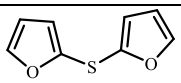	80	255

[a]**Reaction conditions:** Thiol (1 mmol), halide derivative (1 mmol), *t*BuOK (1mmol), FBV-2 (20 mg), acetonitrile (5 ml), 20W LED light (λ = 415 nm), temperature (26-28 ºC) and 1 atm pressure, [b] determined by GC-MS; [c] quantified by GC-FID

The presence of Fe_3O_4 makes the FBV-2 composite magnetically separable; hence the catalyst could easily be recovered after the reaction by an external magnet and used for the subsequent recycling runs. The active photocatalyst FBV-2 was stable over five cycles of photocatalytic reactions (Figure 8). The yield of the diphenyl disulfide with the recovered photocatalyst after fourth run remained 91.4% that was nearly equivalent to that of the fresh photocatalyst (92%). Further, we characterized the spent photocatalyst recovered after the fourth run by XRD to check the structural stability of the material (Fig. S2). The similar diffraction pattern of both the materials (fresh and recovered) indicates the robust nature and structural stability of the catalyst.

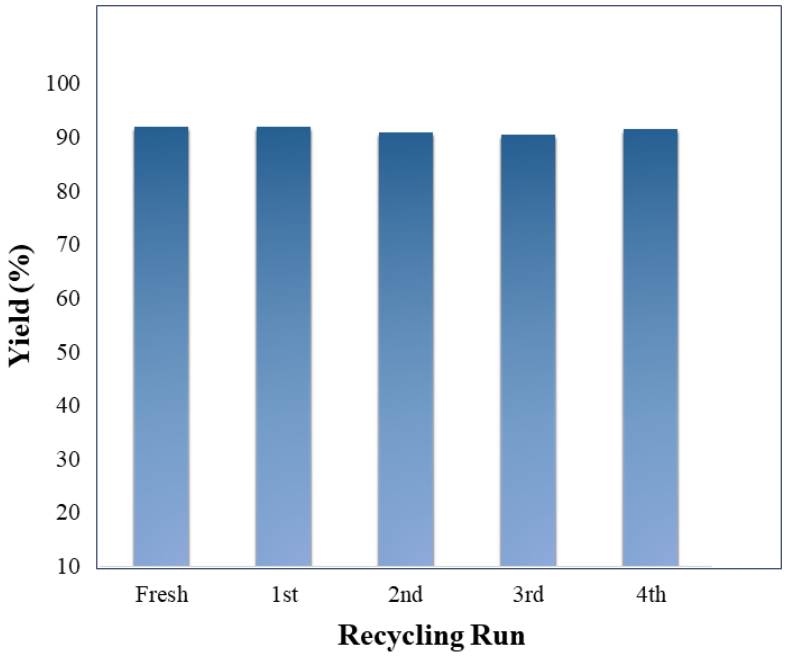

Figure 8: Recyclability of photocatalyst FBV-2

Possible reaction mechanism

The exact mechanism of the reaction is not known at this stage. To understand the possible mechanism of the reaction, the potential values of the conduction band (CB) and valence band (VB) of $BiVO_4$ and Fe_3O_4 were estimated by using the following empirical equations:

$$E_{CB} = X - Ec - 0.5\ Eg \quad (1)$$

$$Eg = E_{VB} - E_{CB} \quad (2)$$

E_{CB} is the CB edge potential, E_{VB} is the VB edge potential, X is the absolute electronegativity of the semiconductor. X for $BiVO_4$ and Fe_3O_4 are 6.035 eV and 5.77 eV respectively.[47-48] E_C = 4.5 eV is the scaling factor relating to the normal hydrogen electrode scale (NHE) to absolute vacuum scale.[49] Using the above equations, the calculated values of CB and VB for Fe_3O_4 was found to be 0.56 eV & 1.98 eV, respectively; whereas the values for $BiVO_4$ were 0.30 eV and 2.77 eV respectively. Therefore, based on the band gap positions of the CB and VB of $BiVO_4$ and Fe_3O_4 in the composite FBV-2, we confirmed the formation of Type I heterojunction and charge carriers (electron and hole) flow from $BiVO_4$ to Fe_3O_4.[50] Accordingly, a hypothesised mechanism for this system is illustrated in Scheme 3. At first, under the light irradiation, charge separation occurred on the surface of the $BiVO_4$ and electrons from the conduction band (CB) being at higher potential transferred to the CB of Fe_3O_4 and subsequently used for the reduction of CO_2 to corresponding CO_2 anion radical. Further, the surface adsorbed thiol (RSH) got oxidized by the photogenerated holes in the VB of Fe_3O_4 to produce corresponding thiol radical cation. Subsequently, the coupling of the thiol radicals provided disulfide and the derived electrons and protons were used for the photoreduction of CO_2 to produce CH_3OH to complete the redox cycle (Scheme 3).

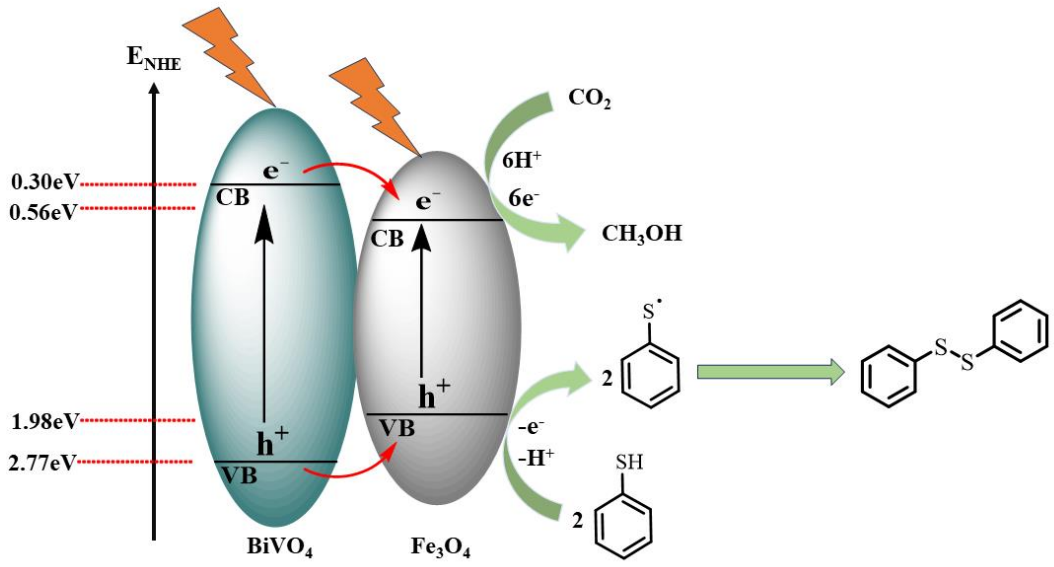

Scheme 3: Possible reaction mechanism for disulfide synthesis over FBV composites

Further to probe the active reaction species, such as electron, hole or electron, we performed the following quenching experiments:

- The addition of small amount of sodium sulphite (0.02 mmol) in the reaction mixture of thiophenol in acetonitrile under optimized reaction conditions resulted to a significant decrease in the yield of the diphenyl disulfide from 92% to 13%. This result confirmed that the photogenerated holes are the key oxidizing agents for the oxidation of thiophenol to disulfide.
- In the subsequent experiment, the addition of electron scavenger silver nitrate (0.02 mmol) resulted to the significant decrease in the methanol yield i.e. 154 μmol/g, indicating the quenching of the photogenerated electrons which are the key species for the reduction of CO_2 to methanol.
- Third, control experiment indicated that the addition of a small amount of radical scavenger 2,2,6,6-tetramethyl-1-piperidinyloxy (TEMPO) into the reaction system inhibited the production of both CH_3OH and disulfide, indicating the reaction proceeded *via* radical intermediates.

Conclusion

We have demonstrated a dual functional system in which CO_2 photoreduction was integrated with the oxidative homocoupling of thiols to disulfides and cross coupling with organo halides to thioethers over a nanostructured photocatalyst composed of iron(III) oxide and bismuth vanadate ($Fe_3O_4/BiVO_4$) under visible light irradiation. The approach was shown to be more broadly applicable to a range of thiols, with high yields obtained. This novel integrated approach provides the efficient utilization of the photogenerated electrons and holes, enabling to produce methanol and value added coupled product in a single reaction system. The development of such dual functional catalytic systems for CO_2 valorization integrated with organics upgrading may open new opportunities for utilization of CO_2 as a sustainable feedstock for chemical production.

Acknowledgement

Director CSIR-Indian Institute of Petroleum, Dehradun, is kindly acknowledged for allowing us to publish these data. NS kindly acknowledge UGC, New Delhi, India & SS are grateful to the Council of Scientific and Industrial Research, New Delhi, India, for financial support. Analytical division of IIP are acknowledged for providing analytical assistance.

References

1. A. J. Hunt, E. H. Sin, R. Marriott and J. H. Clark, *ChemSusChem: Chemistry & Sustainability Energy & Materials*, 2010, **3**, 306-322.
2. R. Wennersten, Q. Sun and H. Li, *Journal of Cleaner Production*, 2015, **103**, 724-736.
3. N. Zhang, D. Zhang, J. Zuo, T. R. Miller, H. Duan and G. Schiller, *Renewable and Sustainable Energy Reviews*, 2022, **169**, 112920.
4. X. Xiong, Y. Zhao, R. Shi, W. Yin, Y. Zhao, G. I N Waterhouse, T. Zhang, Sci. Bull., 2020, 65 (12), 987-994
5. Y. Zhao, G. Chen, T. Bian, C. Zhou, G. I. N. Waterhouse, L-Z. Wu, C.-H. Tung, L. J. Smith, D. O'Hare, T. Zhang, Adv.Mater.2015, 27, 7824–7831
6. Yuan H., Mei J.-H., Gong Y.-N., Zhong D.-C., Lu T.-B. Tungsten. 2023:1–12 (doi.org/10.1007/s42864-023-00208-2)
7. X. Sun, S. Jiang, H. Huang, H. Li, B. Jia and T. Ma, *Angewandte Chemie International Edition*, 2022, **61**, e202204880.
8. S. Wang, L. Wang, D. Wang and Y. Li, *Energy & Environmental Science*, 2023.
9. S. Yoshino, T. Takayama, Y. Yamaguchi, A. Iwase and A. Kudo, *Accounts of chemical research*, 2022, **55**, 966-977.
10. Y.-L. Li, A.-J. Li, S.-L. Huang, J. J. Vittal and G.-Y. Yang, *Chemical Society Reviews*, 2023, **52**, 4725-4754.
11. Q. Guo, F. Liang, X.-B. Li, Y.-J. Gao, M.-Y. Huang, Y. Wang, S.-G. Xia, X.-Y. Gao, Q.-C. Gan and Z.-S. Lin, *Chem*, 2019, **5**, 2605-2616.
12. L. Xiong and J. Tang, *Advanced Energy Materials*, 2021, **11**, 2003216.
13. J. Fu, K. Jiang, X. Qiu, J. Yu and M. Liu, *Materials Today*, 2020, **32**, 222-243.
14. A. Sharma, I. Kaur, D. Dheer, M. Nagpal, N. Bhandari, P. Kumar, D. N. Venkatesh, V. Puri and I. Singh, *Carbohydrate Polymers*, 2022, 120448.
15. S. Chander, G. T. Kulkarni, N. Dhiman and H. Kharkwal, *Frontiers in Chemistry*, 2021, **9**, 573748.
16. B. J. Tombling, C. K. Wang and D. J. Craik, *Angewandte Chemie International Edition*, 2020, **59**, 11218-11232.
17. R. P. Mahapatra, S. S. Srikant, R. B. Rao and B. Mohanty, *Sādhanā*, 2019, **44**, 1-10.
18. L. Lombardi, E. Carnevale and A. Corti, *Waste management*, 2015, **37**, 26-44.
19. X. Dong, H. Hao, F. Zhang and X. Lang, *Journal of Colloid and Interface Science*, 2022, **622**, 1045-1053.
20. K. Y. D. Tan, G. F. Teng and W. Y. Fan, *Organometallics*, 2011, **30**, 4136-4143.
21. S. S. Shah, S. Karthik and N. P. Singh, *RSC Advances*, 2015, **5**, 45416-45419.
22. A. Talla, B. Driessen, N. J. Straathof, L. G. Milroy, L. Brunsveld, V. Hessel and T. Noël, *Advanced Synthesis & Catalysis*, 2015, **357**, 2180-2186.
23. X. B. Li, Z. J. Li, Y. J. Gao, Q. Y. Meng, S. Yu, R. G. Weiss, C. H. Tung and L. Z. Wu, *Angewandte Chemie*, 2014, **126**, 2117-2121.
24. E. Marsault and M. L. Peterson, *Journal of medicinal chemistry*, 2011, **54**, 1961-2004.
25. P. Chauhan, S. Mahajan and D. Enders, *Chemical reviews*, 2014, **114**, 8807-8864.
26. X. Wang, G. D. Cuny and T. Noël, *Angewandte Chemie*, 2013, **125**, 8014-8018.
27. M. Jiang, H. Li, H. Yang and H. Fu, *Angewandte Chemie International Edition*, 2017, **56**, 874-879.
28. A. M. Awwad and N. M. Salem, *Nanoscience and Nanotechnology*, 2012, **2**, 208-213.
29. O. F. Lopes, K. T. Carvalho, A. E. Nogueira, W. Avansi Jr and C. Ribeiro, *Applied catalysis B: environmental*, 2016, **188**, 87-97.
30. A. Zhang and J. Zhang, *Materials Letters*, 2009, **63**, 1939-1942.

31. Z. J. Zhang, X. Y. Chen, B. N. Wang and C. W. Shi, *Journal of crystal growth*, 2008, **310**, 5453-5457.
32. M. Mahdavi, M. B. Ahmad, M. J. Haron, F. Namvar, B. Nadi, M. Z. A. Rahman and J. Amin, *Molecules*, 2013, **18**, 7533-7548.
33. H. H. Bahjat, R. A. Ismail and G. M. Sulaiman, 2021.
34. R. L. Frost, D. A. Henry, M. L. Weier and W. Martens, *Journal of Raman Spectroscopy: An International Journal for Original Work in all Aspects of Raman Spectroscopy, Including Higher Order Processes, and also Brillouin and Rayleigh Scattering*, 2006, **37**, 722-732.
35. A. Fatemi, M. Mozaffari and M. Ghoshani, *Journal of Superconductivity and Novel Magnetism*, 2021, **34**, 2471-2477.
36. G. Xu, M. Du, T. Li, Y. Guan and C. Guo, *Separation and Purification Technology*, 2021, **275**, 119157.
37. F. Chen, Q. Yang, X. Li, G. Zeng, D. Wang, C. Niu, J. Zhao, H. An, T. Xie and Y. Deng, *Applied Catalysis B: Environmental*, 2017, **200**, 330-342.
38. A. A. Majeed and R. T. Rasheed, *J. Appl. Sci. Nanotech*, 2022, **2**, 166-181.
39. A. Kumar, G. Sharma, M. Naushad, A. Kumar, S. Kalia, C. Guo and G. T. Mola, *Journal of Photochemistry and Photobiology A: Chemistry*, 2017, **337**, 118-131.
40. Y. Zhai, Y. Yin, X. Liu, Y. Li, J. Wang, C. Liu and G. Bian, *Materials Research Bulletin*, 2017, **89**, 297-306.
41. G. Zhu, M. Hojamberdiev, W. Que and P. Liu, *Ceramics International*, 2013, **39**, 9163-9172.
42. X. Zhao, C. Yi, M. Zhang, C. Ma, C. Li and Y. Yan, *Journal of Nanoscience and Nanotechnology*, 2018, **18**, 4675-4683.
43. L. Wan, D. Yan, X. Xu, J. Li, T. Lu, Y. Gao, Y. Yao and L. Pan, *Journal of Materials Chemistry A*, 2018, **6**, 24940-24948.
44. L. Cao, D. Ma, Z. Zhou, C. Xu, C. Cao, P. Zhao and Q. Huang, *Chemical Engineering Journal*, 2019, **368**, 212-222.
45. R. Yang, Z. Zhu, C. Hu, S. Zhong, L. Zhang, B. Liu and W. Wang, *Chemical engineering journal*, 2020, **390**, 124522.
46. A. Mishra, V. Verma, A. Khan and A. K. Sinha, *ChemPhotoChem*, 2023, **7**, e202300030.
47. Gao, X.; Bai, Z.; Zhang, S.; Liu, J.; Li, Z., *RSC advances* **2020,***10* (73), 45067-45075.
48. Aguinaco, A.; Mánuel, J. M.; Blanco, E.; Domínguez, M.; Litrán, R.; Delgado, J. J.; Ramírez-del-Solar, M., *Materials* **2022,***15* (19), 6718.
49. Jiang, L.; Fernandez-Garcia, S.; Tinoco, M.; Yan, Z.; Xue, Q.; Blanco, G.; Calvino, J. J.; Hungria, A. B.; Chen, X., *ACS Applied Materials & Interfaces* **2017,***9* (22), 18595-18608.
50. Balapure, A.; Dutta, J. R.; Ganesan, R. *RSC Appl. Interf.*, **2024**, 1, 43-69.